Biomedical Signal Processing and Control 104 (2025) 107481

Contents lists available at ScienceDirect

Biomedical Signal Processing and Control

journal homepage: www.elsevier.com/locate/bspc

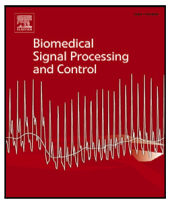

SHARM: Segmented Head Anatomical Reference Models

Essam A. Rashed [a,b,*], Mohammad Al-Shatouri [c], Ilkka Laakso [d], Sachiko Kodera [e,f], Akimasa Hirata [e,f]

[a] Graduate School of Information Science, University of Hyogo, Kobe 650-0047, Japan
[b] Advanced Medical Engineering Research Institute, University of Hyogo, Himeji 670-0836, Japan
[c] Radiology Department, Faculty of Medicine, Suez Canal University, Ismailia 41522, Egypt
[d] Department of Electrical Engineering and Automation, Aalto University, Espoo, Finland
[e] Department of Electrical and Mechanical Engineering, Nagoya Institute of Technology, Nagoya 466-8555, Japan
[f] Center of Biomedical Physics and Information Technology, Nagoya Institute of Technology, Nagoya 466-8555, Japan

ARTICLE INFO

Keywords:
Human head models
Brain segmentation
Convolutional neural networks
MRI

ABSTRACT

Reliable segmentation of anatomical tissues in the human head is a crucial step in various clinical applications, including brain mapping, surgery planning, and computational simulation studies. Segmentation involves identifying different anatomical structures by labeling various tissues using different medical imaging modalities. While the segmentation of brain structures has seen significant progress, non-brain tissues receive less attention due to anatomical complexity and difficulties in observation using standard medical imaging protocols. The lack of comprehensive head segmentation methods and large segmented datasets limits variability studies, particularly in computational evaluations of electrical brain stimulation (neuromodulation), protection from electromagnetic fields, and electroencephalography, where non-brain tissues are essential.

To address this gap, this study introduces the open-access Segmented Head Anatomical Reference Models (SHARM), comprising 196 subjects. These models are segmented into 15 different tissues: skin, fat, muscle, skull cancellous bone, skull cortical bone, brain white matter, brain gray matter, cerebellum white matter, cerebellum gray matter, cerebrospinal fluid, dura, vitreous humor, lens, mucous tissue, and blood vessels. The segmented head models are generated using the open-access IXI MRI dataset and a convolutional neural network structure named ForkNet$^+$. Results indicate high consistency in the statistical characteristics of different tissue distributions across ages compared to real measurements. Electromagnetic exposure studies demonstrate variability in specific absorption rate (SAR) values among subjects. SHARM is expected to be a valuable benchmark for electromagnetic dosimetry studies and various human head segmentation applications.

1. Introduction

Anatomical reference models of human subjects play a crucial role in numerous computer simulation studies, which span a variety of fields such as medical imaging, dosimetric evaluation for diagnostic and therapeutic purposes, and ensuring human safety. These models are fundamentally important because they provide a digital representation of human anatomy, which is mainly generated from imaging data of real individuals. This digital representation allows for a better understanding of real physical effects, making it easier to predict and analyze outcomes through simulation studies. In the field of non-invasive electrical and magnetic stimulation, personalized electrode positions or coil locations are studied extensively. Group-level optimization, as explored in [1,2], aims to refine these techniques for broader applications, ensuring that they are effective across different individuals within a population. Moreover, variability analysis is a key component in these studies. This analysis helps researchers understand the limits of human protection from electromagnetic fields. By examining how different variables affect the outcomes. Human safety standards and guidelines that protect individuals from potential harm due to exposure to electromagnetic fields is mainly based on digital human models [3,4].

Several attempts provided different models that represent whole body models [5–10]. Segmentation of brain tissues is of high interest in several clinical applications such as diagnosis of abnormalities, assessment of neurophysiological performance, surgery planing and many others. Most of standard medical imaging applications can represent brain tissues in high contrast which enable accurate automatic annotation [11]. However, segmentation of non-brain tissues is challenging

* Corresponding author at: Graduate School of Information Science, University of Hyogo, Kobe 650-0047, Japan.
E-mail address: rashed@gsis.u-hyogo.ac.jp (E.A. Rashed).

https://doi.org/10.1016/j.bspc.2024.107481
Received 19 January 2024; Received in revised form 11 July 2024; Accepted 27 December 2024

as it represented in low contrast and/or allocated in limited regions. Moreover, in clinical medical applications, imaging protocols are usually adjusted such that brain tissues are presented in high quality as the main target of diagnostic applications [12]. For reliable electromagnetic brain stimulation and exposure scenarios is it important to use realistic models that represent different human anatomy [13,14].

Whole head segmentation have been discussed mainly for the development of digital models for electromagnetic stimulation studies. SimNibs is an open source software for the simulation of non-invasive brain stimulation that include magnetic resonance (MR) image segmentation to generate head models [15,16]. However, segmentation is limited to major head tissues such as white matter (WM), grey matter (GM), cerebrospinal fluid (CSF), skull and scalp. ROAST is another pipeline the include automatic MRI segmentation based on SPM12 [17] with variety of segmentation and electromagnetic modeling options [18]. However, ROAST segmentation is also limited to a few number of tissues as in Table 1 in [18]. Segmentation of fifteen head tissues using multi-modality images (MRI T1/T2, mDixon, venogram and CT) is proposed in [19]. Recently, the use of deep learning architectures demonstrate quality improvement of anatomical segmentation [20]. Several network architectures such as ForkNet [21], SubForkNet [22] and FastSurfer [23] have been used to generate human head models with different scope and applications.

Due to the complexity of full head segmentation and requirements of intensive efforts for manual parameters adjustment, there is a shortage of relatively large dataset of human head models. This problem becomes more feasible with the use of deep learning as robust segmentation tool with superior accuracy compared to conventional methods. The aim of this work is to generate an open-access Segmented Head Anatomical Reference Models (SHARM) that is large enough for subject variability studies. The developed dataset consists of 196 subjects segmented into 15 different tissues. It is worth noting that the network architecture, ForkNet$^+$, that is used to compute SHARM is an extension of our earlier study in [21]. The main contributions of this study can be summarized as follows:

- An open-source deep learning pipeline for automatic segmentation of MRI head images.
- An open-access large human head dataset segmented into brain and non-brain tissues.
- Evaluation of the consistency of segmented models with realistic tissue characteristics.
- Validation of segmented models using electromagnetic exposure scenarios with 2 and 6 GHz.

2. Materials and methods

2.1. Dataset and general pipeline

The MRI dataset used in this study is the IXI Dataset[1] which consists of around 600 MRI scans of healthy subjects. A set of 196 subjects are selected (123 females, 70 males, and 3 unknown), that are imaged at two hospitals (100 were imaged at the Guy's Hospital (London, UK) with Philips 1.5T system and 96 were images at the Hammersmith Hospital (London, UK) using a Philips 3T system). Excluded images criteria are based on quality of the image and availability of multimodlity scans. The T1w/T2w image data are in Nifti formats and are used for generation of the head models.

The raw T1 and T2-weighted MR images are registered using BrainsFit [24] such that T2w are adjusted to fit with T1w. The acoustic noise is reduced through contouring of head surface and relabeling external region as air voxels. The N4 bias field correction method (ITK[2]) is used for bias correction of both MRI modalities. Both T1w/T1w images are normalized with zero mean and unit variance, then scaled to vales [0.01, 0.99]. All the above pre-processing procedures are used to generate the network input volumes (a set of two 256^3 volumes representing T1w/T2w MRI with unified 1^3 mm resolution). A selected set of the network input is segmented into 15 different head tissues using the semi-automatic method detailed in [1]. The segmentation binary labels are used as network target (output) through training process. The remaining subjects are evaluated using trained network to automatically generate segmentation labels. Finally, an aggregation process is used to combine different segmentation labels into a head model. The pre-processed MR scans and segmented head models are available for each subject in SHARM dataset. The data processing pipeline is shown in Fig. 1.

2.2. Semi-automatic segmentation

The target dataset for the training process was generated using a semi-automatic segmentation pipeline that segments T1- and T2-weighted MR image data into 15 tissue types [1]. Briefly, after bias correction and normalization of the MR data, an experienced investigator uses the pipeline to split the head into three compartments: inner compartment, consisting of the volume inside the inner surface of the skull; middle compartment, consisting of the skull and nasal cavity; and the outer compartment, consisting of the volume between the outer surface of the skull and the outer surface of the skin. The investigator verifies the quality of each compartment by visual inspection and, whenever necessary, tunes the control parameters manually until the compartments match the MR data. The contents of the compartments are further segmented automatically, with possible manual tuning, as described in the following.

The inner compartment is segmented into brain using FreeSurfer image analysis software [25,26]. The brain segmentation consists of cerebral gray matter, cerebral white matter, cerebellar gray matter, cerebellar white matter, deep brain structures (brainstem, accumbens, amygdala, caudate, hippocampus, pallidum, putamen, thalamus), and ventricular CSF. The remaining non-brain volume in the inner compartment is segmented into CSF (bright T2-weighted image), blood (dark T2), and dura (non-brain non-CSF tissue close to the inner boundary of the skull). Anterior and middle cerebral arteries initially estimated from T2 are corrected using thresholding of registered MRA images (when available). Deep brain structures are treated as GM. The middle compartment consisting of the skull is segmented into cortical and cancellous bone by thresholding the T2-weighted MRI data. It is ensured that the inner and outer cortical bone layers are at least 1 mm and 1.5 mm thick, respectively. The nasal cavity also belongs to the middle compartment and is segmented as either mucous tissue or cortical bone based on T2-weighted images. The outer compartment is segmented into skin, fat, muscle, and eyes. The scalp (including subcutaneous fat) is segmented as the outer layer of the head, with thickness between 2 mm and 10 mm. Fat and muscle are segmented based on thresholding the T1-weighted image data. Finally, eyes and lens are segmented using both T1- and T2-weighted image data.

The resulting segmentation has uniform voxel size of 0.5 mm × 0.5 mm × 0.5 mm, half of that of the input MR images. In this study, the segmented dataset was downscaled to the same resolution as the input images using three-dimensional nearest neighborhood interpolation algorithm.

2.3. Network architecture

The deep learning architecture used here is an extension of ForkNet [21] by considering input data from both T1- and T2-weighted MRI scans. We then refer to the new network as ForkNet$^+$. The network inputs are the MRI scans in two encoders and outputs are N decoders each assigned to single anatomical structure (here N=15). The details

[1] http://brain-development.org/ixi-dataset/
[2] https://itk.org/

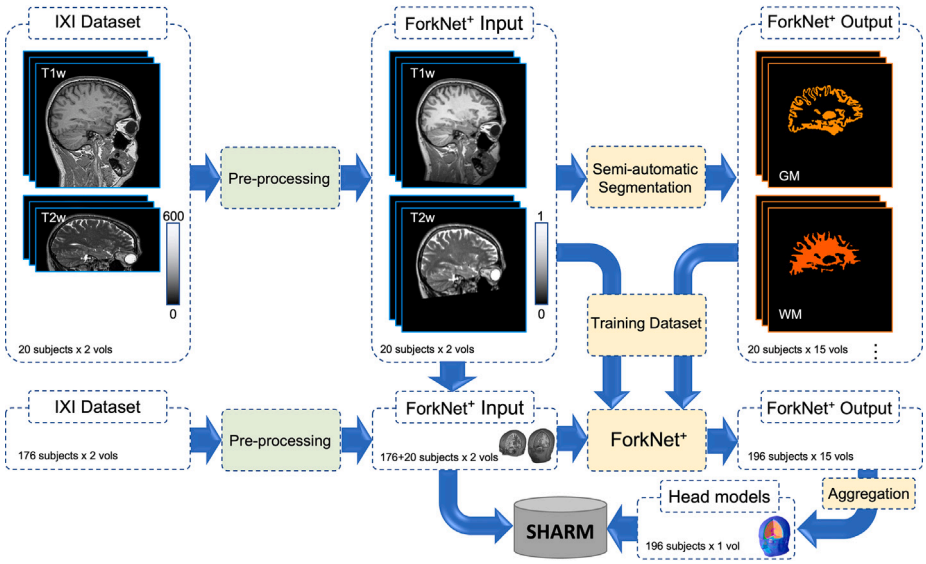

Fig. 1. Data flow used to generate SHARM from IXI dataset.

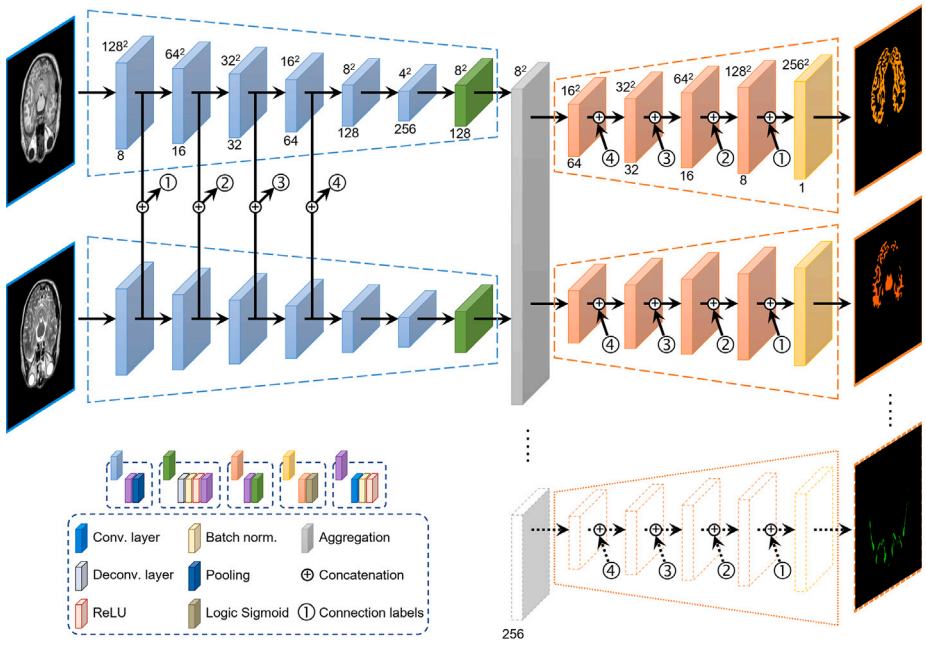

Fig. 2. ForkNet+ with MRI T1w/T2w inputs and N segmented tissues outputs.

of the layer structures and data processing flow is shown in Fig. 2. The network output are binary masks that identify different anatomical tissues/liquids such as skin, muscle, fat, skull (cortical bone), skull (cancellous bone), CSF, blood vessels, dura, brain GM, brain WM, cerebellum GM, cerebellum WM, vitreous humor, eye lens, mocous tissue and whole head. ForkNet+ design is flexible and easy to be adjusted to segmented specific number of tissues for different applications as each tissue is segmented using separate decoder (Fig. 2). This network architecture would involve 47K parameters with a convolution kernel of 3×3.

2.4. Head model generation

Once the network is well-trained, the head models are generated through fast evaluation process. To reduce artifacts caused by 2D slice segmentation, a set of three networks are trained using slices of axial, sagittal and coronal directions as shown in Fig. 3. A rule-based segmentation merge approach using majority vote is used to generate the final segmentation from different slicing directions. When no majority in a voxel is found, the neighborhood majority vote [22]. Consider M^{T_1} and M^{T_2} as the volumetric MRI data with K slices used as inputs. The network output (probability maps) represents N segmented

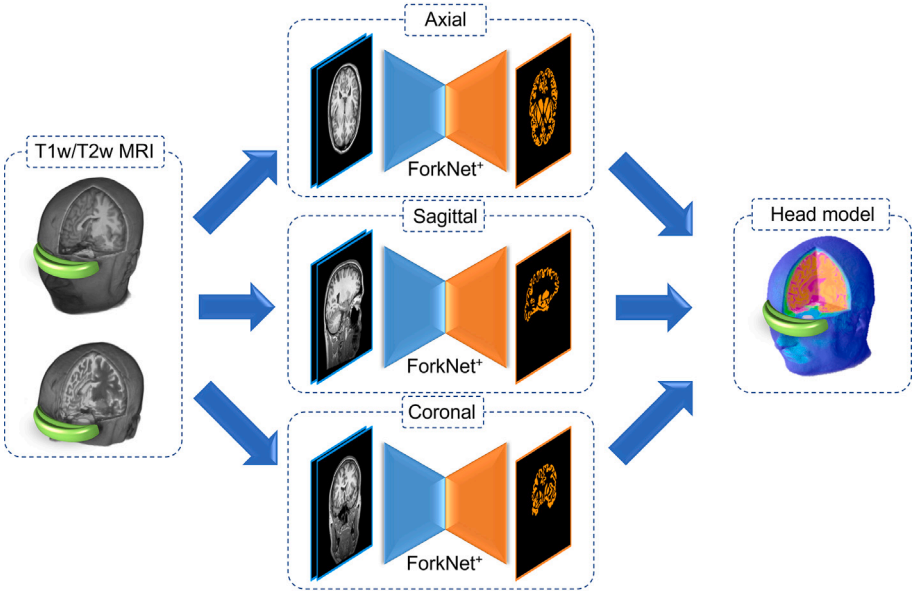

Fig. 3. Network evaluation through different direction to generate the head model.

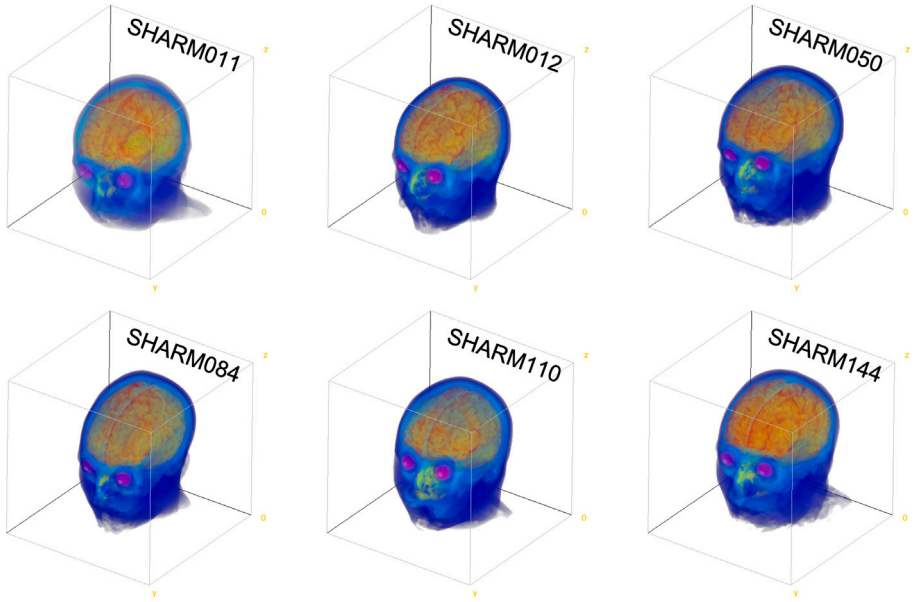

Fig. 4. Volume rendering sample of generated head models.

tissues is computed as follows:

$$L_{k,n} = \text{ForkNet}^{+}(M_k^{T_1}, M_k^{T_2}),\ k = 1, \ldots\ K;\ n = 1, \ldots, N. \tag{1}$$

The corresponding segmented slice is computed using the following Softmax rule:

$$R_k(i,j) = \begin{cases} \arg\max_n L_{k,n}(i,j) & \max_n L_{k,n}(i,j) >= \epsilon \\ 0 & \max_n L_{k,n}(i,j) < \epsilon \end{cases} \tag{2}$$

where $\epsilon = 0.3$ is a background threshold value. A rule-based segmentation merge approach is used for generate the final segmentation from different slicing directions (axial, sagittal, and coronal) as follows:

$$R_k^*(i,j) = \arg \max_{t=a,s,c} \max_n \text{Count}_{i,j\in\Omega} R_k^t(i,j), \tag{3}$$

where R^a, R^s, and R^c are segmentation results obtained from axial, sagittal, and coronal directions, respectively and Ω =3 × 3 is a local neighborhood region.

3. Results

3.1. Dataset generation

A set of 20 randomly selected head models and associated segmented labels are used to train ForkNet+. The network architecture is developed using Wolfram Mathematica (R) ver. 13.0, installed on a Ubuntu 20.04 workstation of 12 Cores Intel (R) Core (TM) i9-10920X @3.50 GHz, 64 GB memory, and NVIDIA RTX A6000 GPU. A three networks (axial, sagittal and coronal) are trained with cross-entropy loss function and ADAM optimization algorithm. The training was considered using 50 epochs with batch size 4. To reduce the computation cost, the number of output tracks is set to $N = 4$ (i.e., a set of 4 tissues are trained simultaneously). A single training round requires about 24 mins and testing of single tissue requires about 14 secs.

The remaining 176 head models are evaluated through trained networks and the network output is aggregated to generate the head

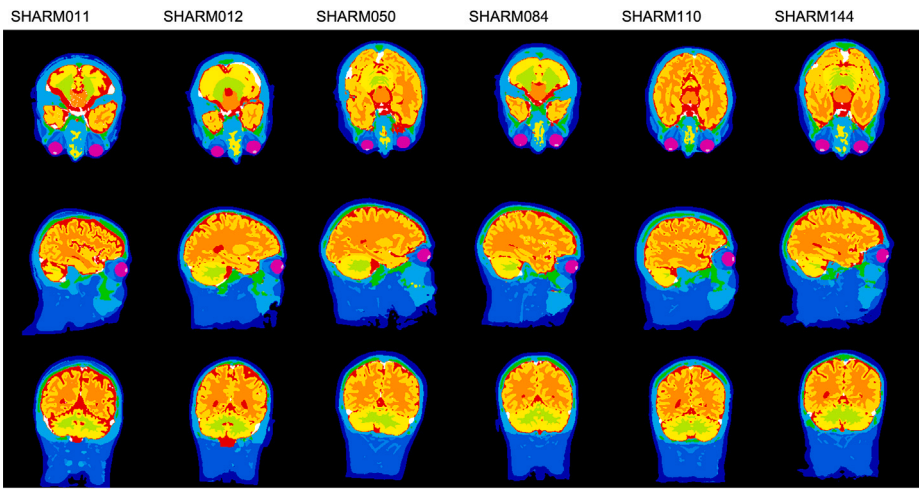

Fig. 5. Axial, sagittal and coronal slices (top to bottom) of head models shown in Fig. 4 in order.

models. Example of generated head models are shown in Figs. 4 and 5. In some few cases, some manual edition is required mainly to remove a small regions of CSF-like tissue uncorrected segmented inside the mouth. Some other cases are excluded due to the strong noise that is difficult to be automatically removed and lead to incorrect segmentation of external contour. Evaluation of segmentation accuracy is not conducted due to the lack of manual true annotation and it is out of the scope of this work. However, we provide quantitative assessment of different tissues of the SHARM dataset. In principle, we study the variability of segmented volumes within age scale to validate the validity of SHARM models.

Fig. 6 demonstrates a regression curves of segmented brains. Brain is considered as a composition of GM, WM and CSF. It shows that a decline in global GM volume with age (R^2=0.274), while there is no significant change in WM volume with age (R^2=0.001). A remarkable increase in CSF volume with age (R^2=0.277). Difference between gender grouping and percentage of different structures with respect to total intracranial volume (TIV) are also shown in Fig. 6 and it is consistent with results reported in literature (e.g., [27–29]). The change in TIV over age and the correlation between GM/WM ratio with age is shown in Fig. 7. The change of skin, muscle, fat, skull, vitreous humor, and eye lens volumes is shown in Fig. 8. In general the volume of skin, muscles, and fat tissues are increasing with aging. Skull and eye lens does not change so much while the volume of vitreous humor is shrinked as reported earlier [30]. Data shown in Fig. 9 demonstrate that the volume of brain is highly correlated with the body mass index (BMI) and brain volume of male subjects are of large volume compared with females [31]. SHARM dataset can be download[3] in MATLAB (*.mat) files.

3.2. Evaluation of ForkNet$^+$

To validate the performance of ForkNet$^+$, we conduct a comparison study against Vanilla Unet [32], UNet++ [33], MultiResUNet [34], DCSAU-Net [35] and original ForkNet [36]. All models are trained using the same 20 subjects and tested using randomly selected 10 subjects. The ground truth is computed using the semi-automatic method [1]. Other training setups remains the same as those in previous section. In case where the network has a single input encoder, such as UNet, the dual modalities are processed as a multi-channels image. Validation is performed using dice coefficient as a metric of segmentation accuracy. This comparison would provide a useful insights on the performance evaluation of all segmented tissues individually as listed in Table 1. Results indicate the ForkNet$^+$ performance very well in almost all tissues except the cases for fat and brain WM, where DCSAU-Net achieve higher performance.

3.3. Electromagnetic computations

One potential application of SHARM is the assessment of electromagnetic exposure within large population. For numerical demonstration, 50 head models were used for evaluating inter-individual variability. A dipole antenna was positioned at a separation distance of 25 mm from the surface of the head model (Fig. 10). The antenna output power was set to 1 W. The frequency considered are 2 and 6 GHz. The 2 GHz was the frequency band where the wireless communications system is used, while the 6 GHz was chosen where the penetration depth becomes small as prescribed in the international guidelines [37]. For electromagnetic analysis, the finite-difference time-domain (FDTD) method [38] was used to compute the internal electromagnetic field in the numerical human head models. The specific absorption rate (SAR) was defined as

$$SAR = \frac{\sigma}{\rho}|\mathbf{E}|^2, \tag{4}$$

where $|\mathbf{E}|$ denotes the root mean square values of the internal electric field, and σ and ρ are the conductivity and mass density of the tissue, respectively. This physical quantity is used as a metric for human protection from radiofrequency exposure greater than 100 kHz [39,40]. The dielectric properties of the tissues were determined with a Cole-Cole dispersion model [41]. Fig. 10 shows the SAR distribution on the horizontal cross section of a head model. The SAR distribution penetrate at deeper region at 2 GHz as compared to 6 GHz. The SAR distribution is not uniform because of the tissue inhomogeneity characterized by the tissue electrical conductivity.

4. Discussion

This work demonstrate a new benchmark dataset for several computational neuroscience applications. The open-access SHARM consists of 196 head models segmented into 15 different tissues that cover a wide range of subject variability. A boxplot demonstrates the volume variations of different structures in SHRAM is shown in Fig. 11. It is clearly observed that skull volume is 0.827 $\pm 0.08L$ (male) and 0.730 $\pm 0.08L$ (female). These values are highly correlated with those listed in the ICRP Reference man (averaged bone without marrow of Skull is 708 gm). The vitreous humor is 15.098 $\pm 2.10mL$ (male) and 14.124 $\pm 1.91mL$ (female) that is referenced as value 15 ± 6.5 gm in adult [42,

[3] https://figshare.com/s/a4d9ba6f18a6b7f7ba2c (zip, 7.62 GB, password: Sharm@2022#)

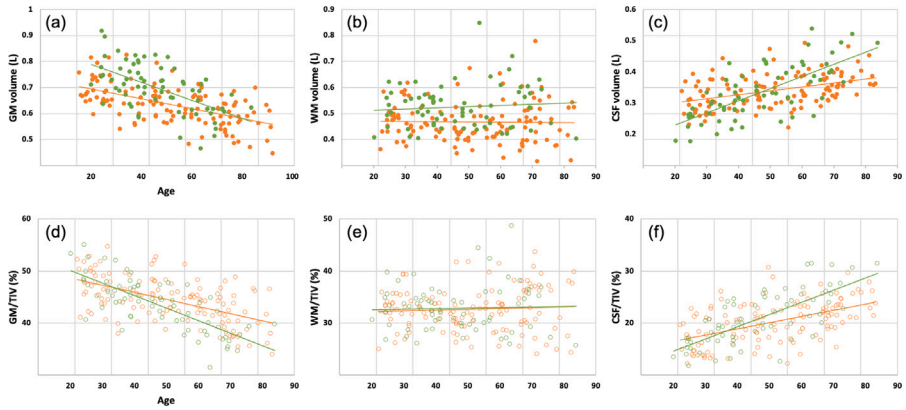

Fig. 6. (a) Regression lines with scatter plot of total GM volume over age for all subjects (female in orange and male in green). (b) and (c) are regression lines and scatter plots for total WM and CSF, respectively. (d)–(f) are the regression lines and scatter plots for fractional volume (with respect to TIV) of GM, WM and CSF, respectively.

Table 1
Mean and standard deviation of dice coefficient values computed for 176 subjects of different network-generated models. Bold indicate superior mean value.

Tissue	UNet	UNet++	MultiResUNet	DCSAU-Net	ForkNet	ForkNet$^+$
Skin	82.54 ± 3.41	84.35 ± 5.16	85.01 ± 6.54	85.01 ± 8.20	87.34 ± 5.43	**89.23** ± 5.13
Muscle	84.98 ± 7.12	87.65 ± 4.56	87.71 ± 5.49	93.54 ± 6.12	92.76 ± 3.52	**93.78** ± 6.34
Fat	81.32 ± 8.54	83.09 ± 7.65	83.15 ± 7.64	**85.34** ± 6.54	84.92 ± 6.78	85.22 ± 5.43
Bone (cancellous)	77.23 ± 8.76	81.34 ± 5.43	79.78 ± 5.09	83.65 ± 4.01	85.65 ± 7.65	**88.42** ± 5.43
Bone (cortical)	84.65 ± 5.45	85.78 ± 6.54	83.87 ± 8.85	87.51 ± 5.01	89.41 ± 5.43	**90.12** ± 5.09
Dura	47.65 ± 10.34	51.65 ± 11.34	52.98 ± 8.87	57.65 ± 9.81	55.50 ± 9.87	**59.11** ± 11.43
Blood	74.51 ± 10.98	73.76 ± 8.87	74.57 ± 9.02	77.76 ± 9.87	78.01 ± 8.21	**82.67** ± 9.11
CSF	88.65 ± 4.65	89.90 ± 3.45	90.55 ± 3.71	91.67 ± 3.29	88.76 ± 8.65	**92.32** ± 3.67
Brain GM	89.11 ± 2.45	91.65 ± 2.89	93.89 ± 7.22	93.76 ± 3.56	94.76 ± 2.11	**94.89** ± 2.87
Brain WM	93.12 ± 3.23	91.43 ± 1.34	92.70 ± 3.49	**95.67** ± 2.11	93.56 ± 5.32	94.98 ± 2.19
Cerebellum GM	92.74 ± 2.21	93.98 ± 1.90	93.70 ± 2.87	94.76 ± 1.11	95.76 ± 1.98	**96.01** ± 0.98
Cerebellum WM	93.84 ± 2.45	93.17 ± 1.77	93.45 ± 2.09	93.77 ± 1.26	94.09 ± 1.38	**95.27** ± 1.54
Vitreous humor	94.54 ± 0.98	94.89 ± 0.93	95.34 ± 1.34	96.41 ± 1.09	96.78 ± 1.77	**97.66** ± 1.06
Eye lens	76.87 ± 15.01	79.08 ± 13.87	75.43 ± 12.15	82.98 ± 9.80	79.34 ± 8.71	**83.12** ± 7.76
Mucous Tissue	72.34 ± 18.01	73.61 ± 15.08	72.57 ± 13.45	75.61 ± 7.81	72.65 ± 8.50	**77.89** ± 8.11

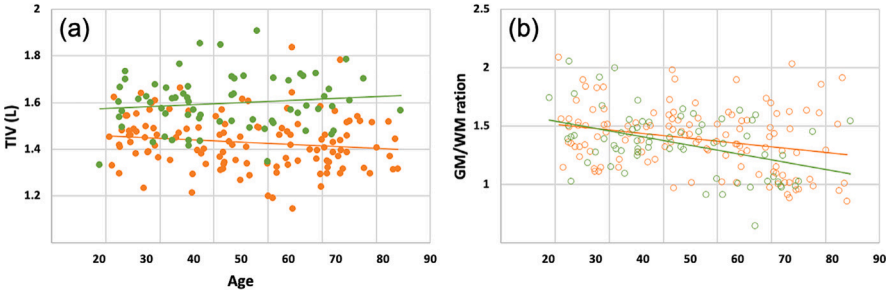

Fig. 7. (a) Regression curves and scatter plot of (a) total intracranial volume (TIV) in liters and (b) GM/WM ratio over age for all subjects.

Table 97, p. 220]. Also, eye lens is 0.246 ± 0.07 mL (male) and 0.242 ± 0.08 mL (female) which is calculated as 172 to 258.1 gm for (20 - 60 y) adult [42, Table 100, p. 225]. Calculated volume and weight of different SHRAM tissues are compared with those reported in [42] in Table 2. These values are example that indicate segmentation accuracy of non-brain tissues.

The segmented models along with normalized T1- and T2-weighted MR scans are available for each subject in additional to other demographic information. Most of the models in SHARM are presented with full head and neck segmentation which enables simulation studies that requires full head models. moreover, the trained deep learning model used to generate SHARM is shared which can be used to generate additional models considering the availability of consistent MR scans. The software ForkNet$^+$ generate individual tissue segmentation in terms of probability maps which enables customized segmentation of a single subject through weighting based aggregation process (similar to those presented in [43]). It is worth noting that evaluation of segmentation accuracy is out of the scope of this work, because earlier version of the ForkNet [21] segmentation have been evaluated.

Fig. 12 shows the dependence of local SAR in the brain on the age and body mass index are shown. Note that the SAR averaged over 10 g of any tissue is used as a metric, while SAR for the brain tissue is considered which is often used for epidemiological study [44]. As shown in Fig. 12(a), SAR is correlated with age at 6 GHz whereas not at 2 GHz. Better correlation was observed in terms of body mass index at 2 and 6 GHz. The tendency of the wave penetration is different at different frequencies. Due to nonlinear coupling with biological tissues, i.e., near-field regime, the field distribution is also affected by the antenna-head separation and the tissue inhomogeneity [45]. In the international guidelines for human protection, reduction factor is applied when setting the limit [37]. To develop different model would be useful when determining such inter-individual variability. Even in

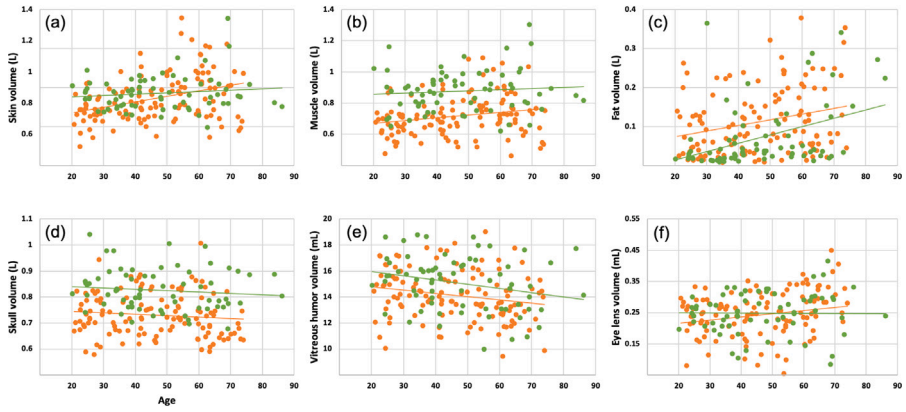

Fig. 8. Regression curves of segmented volume of (a) skin, (b) muscle, (c) fat, (d) skull, (e) vitreous humor, and (f) eye lens in SHARM models.

Table 2
Comparison of volume/weight values of SHARM models with ICRP Reference man [42].

#	Tissue	Density (kg/m^3)[a]	Gender	Volume (mL)		Weight (gm)		Reference value	Comments[b]
1	Brain (GM+WM+CSF)	1041	M F	1437 1277	105 108	1502 1336	110 113	1355 gm 1200 gm	Adult (20–60 y), Table 93
2	Cerebellum	1045	M F	124 115	14 15	130 120	14 16	100–133 gm	Adult (20–90 y), Eq. @ p.212
3	Vitreous humor	1005	M F	15.1 14.1	2.11 1.91	15.172 14.19	2.1 1.9	15 ± 6.5 gm	Table 97
4	Eye lens	1076	M F	0.246 0.242	0.07 0.08	0.264 0.26	0.075 0.086	172–258 mg	Table 100
5	Skull	1908	M F	827 730	79 82	1,578 1393	151 156	706 gm	Table 16

[a] Average density values are acquired from [53].
[b] References from [42].

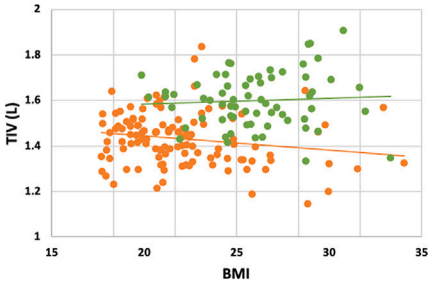

Fig. 9. Regression curves of TIV per BMI.

the epidemiological study for potential adverse health effect, interindividual variability have been considered [44]. In addition, medical applications, such as brain stimulation, the non-brain tissue structure is suggested to be important for dose in the brain [46,47]. In that research field, the number of the models considered are typically limited (less than 20) (e.g., [48–50]), while some attempts have been conducted for group-level analysis recently [51,52]. Our model set would be useful for such group-level analysis.

The limitation of this work is the lack of variability of MR data acquisition. Data are acquired from two scanners installed at two medical institutes but it is developed by the same manufacturer. Further extension with data from other manufacturers are planned to be included in future versions. Moreover, we will include more information considering the segmentation of deep brain structures and fiber orientations in future versions of SHARM. Also, there is a lack of bone structure accuracy in the neck region as lack of neck data in T2 images. In future, we will investigate potential approaches to improve the segmentation neck region properly.

5. Conclusion

In this study, we present SHARM, a benchmark dataset of 196 segmented human head models. The models are segmented into 15 different tissues using a deep learning network named ForkNet$^+$. The freely available models, along with normalized MR T1- and T2-weighted scans, enable large-scale studies in various applications such as electromagnetic brain stimulation. Results demonstrate that the segmented models exhibit high consistency with measurements obtained from real data. One feature of ForkNet$^+$ is that the segmentation of each tissue is generated as probability maps, allowing for parametric segmentation and further customization of the generated head models. The trained networks and source code are shared for potential use in head model generation. With a large sample size and diverse subject ages, SHARM facilitates reliable studies in electromagnetic dosimetry and human safety.

Up to the best of authors' knowledge, the SAR study in Section 3.3 has nor been discussed before due to the lack of wide-scale dataset such as SHARM. This would be the first systematic variation study to demonstrate SAR variability in terms of age, gender and BMI. The openly available dataset would allow the community to use the same models for different types of exposure scenarios, which is very relevant for exposure assessment community and human safety standards.

In the future, additional regions such as deep brain structures will be segmented and added to enable more comprehensive studies of deep brain stimulation. Further studies using SHARM in different brain stimulation scenarios will facilitate a better understanding of various factors such as age, gender, and BMI. This is considered future work. After publication, Mathematica notebooks demonstrate the implementation of ForkNet$^+$ architectures and trained networks will be available for download at: https://github.com/erashed/ForkNetPlus

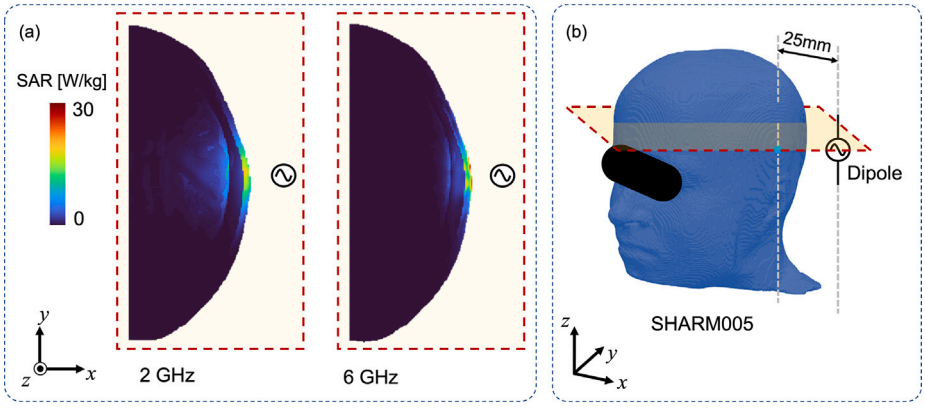

Fig. 10. (a) SAR distribution at 2 and 6 GHz in axial slices obtained from the exposure scenario shown in (b) where the antenna is located 25 mm aside to the head model.

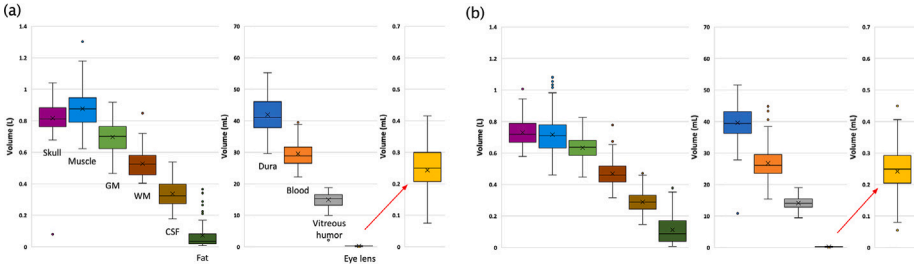

Fig. 11. Boxplot demonstrates volume variations of different structures in SHARM (a) male and (b) female subjects.

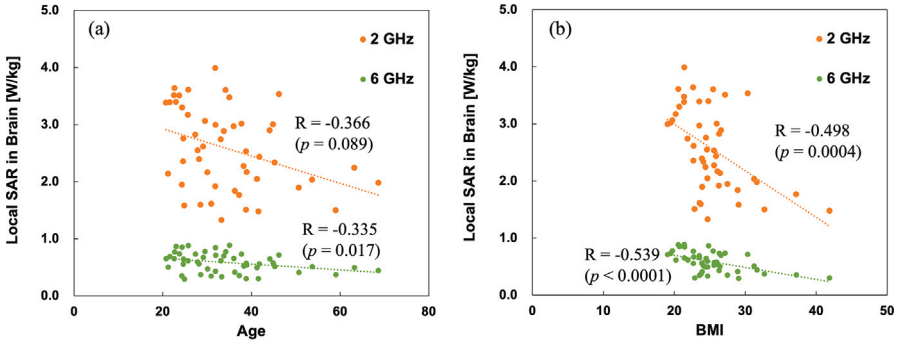

Fig. 12. Dependence of local SAR in brain on (a) age and (b) body mass index.

CRediT authorship contribution statement

Essam A. Rashed: Writing – review & editing, Writing – original draft, Visualization, Supervision, Software, Methodology, Funding acquisition, Data curation, Conceptualization. **Mohammad Al-Shatouri:** Validation, Data curation. **Ilkka Laakso:** Writing – review & editing, Methodology. **Sachiko Kodera:** Validation, Data curation. **Akimasa Hirata:** Writing – review & editing, Supervision, Project administration, Funding acquisition, Conceptualization.

Declaration of competing interest

The authors declare that they have no known competing financial interests or personal relationships that could have appeared to influence the work reported in this paper.

Acknowledgments

This work was funded by the Japan Society for the Promotion of Science (JSPS), a Grant-in-Aid for Scientific Research, Grant number JSPS KAKENHI 22K12765. The authors would like to thank Mr. Itsuki Komine (Nagoya Institute of Technology, Japan) for providing help in Electromagnetic Computations.

Data availability

Data will be made available on request.

References

[1] I. Laakso, S. Tanaka, S. Koyama, V. De Santis, A. Hirata, Inter-subject variability in electric fields of motor cortical tDCS, Brain Stimul. 8 (5) (2015) 906–913, http://dx.doi.org/10.1016/j.brs.2015.05.002.

[2] J. Gomez-Tames, A. Hamasaka, I. Laakso, A. Hirata, Y. Ugawa, Atlas of optimal coil orientation and position for TMS: A computational study, Brain Stimul. 11 (4) (2018) 839–848, http://dx.doi.org/10.1016/j.brs.2018.04.011.

[3] A. Hirata, Y. Diao, T. Onishi, K. Sasaki, S. Ahn, D. Colombi, V. De Santis, I. Laakso, L. Giaccone, W. Joseph, E.A. Rashed, W. Kainz, J. Chen, Assessment of human exposure to electromagnetic fields: Review and future directions, IEEE Trans. Electromagn. Compat. 63 (5) (2021) 1619–1630, http://dx.doi.org/10.1109/TEMC.2021.3109249.

[4] ICNIRP, et al., Gaps in knowledge relevant to the "Guidelines for limiting exposure to time-varying electric and magnetic fields (1 Hz–100 kHz)", Health Phys. 118 (5) (2020) 533–542, http://dx.doi.org/10.1097/HP.0000000000001261.

[5] T. Nagaoka, S. Watanabe, K. Sakurai, E. Kunieda, S. Watanabe, M. Taki, Y. Yamanaka, Development of realistic high-resolution whole-body voxel models of Japanese adult males and females of average height and weight, and application of models to radio-frequency electromagnetic-field dosimetry, Phys. Med. Biol. 49 (1) (2004) 1–15, http://dx.doi.org/10.1088/0031-9155/49/1/001.

[6] C.H. Kim, S.H. Choi, J.H. Jeong, C. Lee, M.S. Chung, HDRK-man: a whole-body voxel model based on high-resolution color slice images of a Korean adult male cadaver, Phys. Med. Biol. 53 (15) (2008) 4093–4106, http://dx.doi.org/10.1088/0031-9155/53/15/006.

[7] A. Christ, W. Kainz, E.G. Hahn, K. Honegger, M. Zefferer, E. Neufeld, W. Rascher, R. Janka, W. Bautz, J. Chen, B. Kiefer, P. Schmitt, H.-P. Hollenbach, J. Shen, M. Oberle, D. Szczerba, A. Kam, J.W. Guag, N. Kuster, The Virtual Family—development of surface-based anatomical models of two adults and two children for dosimetric simulations, Phys. Med. Biol. 55 (2) (2009) N23–N38, http://dx.doi.org/10.1088/0031-9155/55/2/n01.

[8] W.P. Segars, G. Sturgeon, S. Mendonca, J. Grimes, B.M.W. Tsui, 4D XCAT phantom for multimodality imaging research, Med. Phys. 37 (9) (2010) 4902–4915, http://dx.doi.org/10.1118/1.3480985.

[9] D. Yu, M. Wang, Q. Liu, Development of Chinese reference man deformable surface phantom and its application to the influence of physique on electromagnetic dosimetry, Phys. Med. Biol. 60 (17) (2015) 6833–6846, http://dx.doi.org/10.1088/0031-9155/60/17/6833.

[10] W. Kainz, E. Neufeld, W.E. Bolch, C.G. Graff, C.H. Kim, N. Kuster, B. Lloyd, T. Morrison, P. Segars, Y.S. Yeom, M. Zankl, X.G. Xu, B.M.W. Tsui, Advances in computational human phantoms and their applications in biomedical engineering—A topical review, IEEE Trans. Radiat. Plasma Med. Sci. 3 (1) (2019) 1–23, http://dx.doi.org/10.1109/TRPMS.2018.2883437.

[11] C. Baur, S. Denner, B. Wiestler, N. Navab, S. Albarqouni, Autoencoders for unsupervised anomaly segmentation in brain MR images: A comparative study, Med. Image Anal. 69 (2021) 101952, http://dx.doi.org/10.1016/j.media.2020.101952.

[12] P. Kalavathi, V.S. Prasath, Methods on skull stripping of MRI head scan images—a review, J. Digit. Imaging 29 (2016) 365–379, http://dx.doi.org/10.1007/s10278-015-9847-8.

[13] W. Kainz, E. Neufeld, W.E. Bolch, C.G. Graff, C.H. Kim, N. Kuster, B. Lloyd, T. Morrison, P. Segars, Y.S. Yeom, et al., Advances in computational human phantoms and their applications in biomedical engineering—a topical review, IEEE Trans. Radiat. Plasma Med. Sci. 3 (1) (2018) 1–23, http://dx.doi.org/10.1109/TRPMS.2018.2883437.

[14] K. Sasaki, E. Porter, E.A. Rashed, L. Farrugia, G. Schmid, Measurement and image-based estimation of dielectric properties of biological tissues —past, present, and future—, Phys. Med. Biol. 67 (14) (2022) 14TR01, http://dx.doi.org/10.1088/1361-6560/ac7b64.

[15] A. Thielscher, A. Antunes, G.B. Saturnino, Field modeling for transcranial magnetic stimulation: A useful tool to understand the physiological effects of TMS? in: 2015 37th Annual International Conference of the IEEE Engineering in Medicine and Biology Society, EMBC, 2015, pp. 222–225, http://dx.doi.org/10.1109/EMBC.2015.7318340.

[16] G.B. Saturnino, O. Puonti, J.D. Nielsen, D. Antonenko, K.H. Madsen, A. Thielscher, SimNIBS 2.1: A Comprehensive Pipeline for Individualized Electric Field Modelling for Transcranial Brain Stimulation, Cold Spring Harbor Laboratory, 2018, http://dx.doi.org/10.1101/500314, BioRxiv.

[17] J. Ashburner, K.J. Friston, Unified segmentation, Neuroimage 26 (3) (2005) 839–851, http://dx.doi.org/10.1016/j.neuroimage.2005.02.018.

[18] Y. Huang, A. Datta, M. Bikson, L.C. Parra, Realistic volumetric-approach to simulate transcranial electric stimulation—ROAST—a fully automated open-source pipeline, J. Neural Eng. 16 (5) (2019) 056006, http://dx.doi.org/10.1088/1741-2552/ab208d.

[19] O. Puonti, K. Van Leemput, G.B. Saturnino, H.R. Siebner, K.H. Madsen, A. Thielscher, Accurate and robust whole-head segmentation from magnetic resonance images for individualized head modeling, Neuroimage 219 (2020) 117044, http://dx.doi.org/10.1016/j.neuroimage.2020.117044.

[20] Z. Akkus, A. Galimzianova, A. Hoogi, D.L. Rubin, B.J. Erickson, Deep learning for brain MRI segmentation: state of the art and future directions, J. Digit. Imaging 30 (2017) 449–459, http://dx.doi.org/10.1007/s10278-017-9983-4.

[21] E.A. Rashed, J. Gomez-Tames, A. Hirata, Development of accurate human head models for personalized electromagnetic dosimetry using deep learning, Neuroimage 202 (2019) 116132, http://dx.doi.org/10.1016/j.neuroimage.2019.116132.

[22] E.A. Rashed, J. Gomez-Tames, A. Hirata, End-to-end semantic segmentation of personalized deep brain structures for non-invasive brain stimulation, Neural Netw. 125 (2020) 233–244, http://dx.doi.org/10.1016/j.neunet.2020.02.006.

[23] L. Henschel, S. Conjeti, S. Estrada, K. Diers, B. Fischl, M. Reuter, FastSurfer - A fast and accurate deep learning based neuroimaging pipeline, Neuroimage 219 (2020) 117012, http://dx.doi.org/10.1016/j.neuroimage.2020.117012.

[24] H. Johnson, G. Harris, K. Williams, et al., BRAINSFit: mutual information rigid registrations of whole-brain 3D images, using the insight toolkit, Insight J. 57 (1) (2007) 1–10.

[25] A.M. Dale, B. Fischl, M.I. Sereno, Cortical surface-based analysis: I. Segmentation and surface reconstruction, Neuroimage 9 (2) (1999) 179–194, http://dx.doi.org/10.1006/nimg.1998.0395.

[26] B. Fischl, A.M. Dale, Measuring the thickness of the human cerebral cortex from magnetic resonance images, Proc. Natl. Acad. Sci. 97 (20) (2000) 11050–11055, http://dx.doi.org/10.1073/pnas.200033797.

[27] A.N. Ruigrok, G. Salimi-Khorshidi, M.-C. Lai, S. Baron-Cohen, M.V. Lombardo, R.J. Tait, J. Suckling, A meta-analysis of sex differences in human brain structure, Neurosci. Biobehav. Rev. 39 (2014) 34–50, http://dx.doi.org/10.1016/j.neubiorev.2013.12.004.

[28] Y. Ge, R.I. Grossman, J.S. Babb, M.L. Rabin, L.J. Mannon, D.L. Kolson, Age-related total gray matter and white matter changes in normal adult brain. Part I: volumetric MR imaging analysis, Am. J. Neuroradiol. 23 (8) (2002) 1327–1333, URL http://www.ajnr.org/content/23/8/1327.

[29] C.D. Good, I.S. Johnsrude, J. Ashburner, R.N. Henson, K.J. Friston, R.S. Frackowiak, A voxel-based morphometric study of ageing in 465 normal adult human brains, Neuroimage 14 (1) (2001) 21–36, http://dx.doi.org/10.1006/nimg.2001.0786.

[30] J. Sebag, Ageing of the vitreous, Eye 1 (2) (1987) 254–262, http://dx.doi.org/10.1038/eye.1987.45.

[31] L. Eliot, A. Ahmed, H. Khan, J. Patel, Dump the "dimorphism": Comprehensive synthesis of human brain studies reveals few male-female differences beyond size, Neurosci. Biobehav. Rev. 125 (2021) 667–697, http://dx.doi.org/10.1016/j.neubiorev.2021.02.026.

[32] O. Ronneberger, P. Fischer, T. Brox, U-net: Convolutional networks for biomedical image segmentation, in: Medical Image Computing and Computer-Assisted Intervention–MICCAI 2015: 18th International Conference, Munich, Germany, October 5-9, 2015, Proceedings, Part III 18, Springer, 2015, pp. 234–241.

[33] Z. Zhou, M.M.R. Siddiquee, N. Tajbakhsh, J. Liang, UNet++: Redesigning skip connections to exploit multiscale features in image segmentation, IEEE Trans. Med. Imaging 39 (6) (2020) 1856–1867, http://dx.doi.org/10.1109/TMI.2019.2959609.

[34] N. Ibtehaz, M.S. Rahman, MultiResUNet : Rethinking the U-net architecture for multimodal biomedical image segmentation, Neural Netw. 121 (2020) 74–87, http://dx.doi.org/10.1016/j.neunet.2019.08.025.

[35] Q. Xu, Z. Ma, N. H.E., W. Duan, DCSAU-net: A deeper and more compact split-attention U-net for medical image segmentation, Comput. Biol. Med. 154 (2023) 106626, http://dx.doi.org/10.1016/j.compbiomed.2023.106626.

[36] E.A. Rashed, J. Gomez-Tames, A. Hirata, Development of accurate human head models for personalized electromagnetic dosimetry using deep learning, Neuroimage 202 (2019) 116132, http://dx.doi.org/10.1016/j.neuroimage.2019.116132.

[37] ICNIRP, Guidelines for limiting exposure to electromagnetic fields (100 kHz to 300 GHz), Health Phys. 118 (5) (2020) 483–524.

[38] A. Taflove, S.C. Hagness, M. Piket-May, Computational electromagnetics: the finite-difference time-domain method, Electr. Eng. Handb. 3 (629–670) (2005) 15.

[39] ICNIRP, Principles for non-ionizing radiation protection, Health Phys. 118 (5) (2020) 477–482.

[40] IEEE Standards Coordinating Committee, et al., IEEE standard for safety levels with respect to human exposure to radio frequency electromagnetic fields, 0Hz to 300GHz, IEEE (2019).

[41] S. Gabriel, R.W. Lau, C. Gabriel, The dielectric properties of biological tissues: III. Parametric models for the dielectric spectrum of tissues, Phys. Med. Biol. 41 (11) (1996) 2271, http://dx.doi.org/10.1088/0031-9155/41/11/003.

[42] ICRP Publication 23, Reference Man: Anatomical, Physiological and Metabolic Characteristics (Annals of the ICRP), Pergamon Press, Oxford, 1975, URL http://journals.sagepub.com/pb-assets/cmscontent/ANI/P_023_1975_Report_on_the_Task_Group_on_Reference_Man_rev0.pdf.

[43] E.A. Rashed, J. Gomez-Tames, A. Hirata, Influence of segmentation accuracy in structural MR head scans on electric field computation for TMS and tES, Phys. Med. Biol. 66 (6) (2021) 064002, http://dx.doi.org/10.1088/1361-6560/abe223.

[44] A.-K. Lee, S.-E. Hong, J.-H. Kwon, H.-D. Choi, E. Cardis, Mobile phone types and SAR characteristics of the human brain, Phys. Med. Biol. 62 (7) (2017) 2741, http://dx.doi.org/10.1088/1361-6560/aa5c2d.

[45] S.-I. Watanabe, H. Taki, T. Nojima, O. Fujiwara, Characteristics of the SAR distributions in a head exposed to electromagnetic fields radiated by a hand-held portable radio, IEEE Trans. Microw. Theory Tech. 44 (10) (1996) 1874–1883, http://dx.doi.org/10.1109/22.539946.

[46] I. Laakso, S. Tanaka, S. Koyama, V. De Santis, A. Hirata, Inter-subject variability in electric fields of motor cortical tDCS, Brain Stimul. 8 (5) (2015) 906–913, http://dx.doi.org/10.1016/j.brs.2015.05.002.

[47] J. Gomez-Tames, A. Hamasaka, I. Laakso, A. Hirata, Y. Ugawa, Atlas of optimal coil orientation and position for TMS: A computational study, Brain Stimul. 11 (4) (2018) 839–848, http://dx.doi.org/10.1016/j.brs.2018.04.011.

[48] M. Khorrampanah, H. Seyedarabi, S. Daneshvar, M. Farhoudi, Optimization of montages and electric currents in tDCS, Comput. Biol. Med. 125 (2020) 103998, http://dx.doi.org/10.1016/j.compbiomed.2020.103998.

[49] A. Molero-Chamizo, et al., Standard non-personalized electric field modeling of twenty typical tDCS electrode configurations via the computational finite element method: Contributions and limitations of two different approaches, Biol. 10 (12) (2021) http://dx.doi.org/10.3390/biology10121230.

[50] M. Colella, A. Paffi, V.D. Santis, F. Apollonio, M. Liberti, Effect of skin conductivity on the electric field induced by transcranial stimulation techniques in different head models, Phys. Med. Biol. 66 (3) (2021) 035010, http://dx.doi.org/10.1088/1361-6560/abcde7.

[51] K.A. Caulfield, M.S. George, Optimized APPS-tDCS electrode position, size, and distance doubles the on-target stimulation magnitude in 3000 electric field models, Sci. Rep. 12 (1) (2022) 20116.

[52] J. Gomez-Tames, A. Asai, M. Mikkonen, I. Laakso, S. Tanaka, S. Uehara, Y. Otaka, A. Hirata, Group-level and functional-region analysis of electric-field shape during cerebellar transcranial direct current stimulation with different electrode montages, J. Neural Eng. 16 (3) (2019) 036001, http://dx.doi.org/10.1088/1741-2552/ab0ac5.

[53] IT's Foundation, Human body density values, 2023, https://itis.swiss/virtual-population/tissue-properties/database/density/. (Online; Accessed 10 September 2023).